SUMMARY**REPORT**

Laboratory Evaluation of Five Metallic Strand Materials for Corrosion Control of Post-Tensioned Tendons: Summary of Preliminary Findings

FHWA Publication No.: FHWA-HRT-24-158

FHWA Contact: Frank Jalinoos, HRDI-30, 202-493-3082, frank.jalinoos@dot.gov

Researcher: Seung-Kyoung Lee (ORCID ID 0000-0001-7367-5197)

INTRODUCTION

A recent Federal Highway Administration (FHWA) report titled "Corrosion-Induced Durability Issues and Maintenance Strategies for Post-Tensioned Concrete Bridge" reviews corrosion-induced durability issues of post-tensioned (PT) tendons in prestressed concrete bridges.[1] The report discusses corrosion control methods, including using flexible fillers such as petroleum-based microcrystalline wax to replace cementitious grout—an impregnation method using a silicon polymer-based corrosion inhibitor that impregnates the grout to form a barrier to moisture and oxygen upon a pressure-driven injection process—and electrically isolating tendons from surroundings and monitoring their in-service condition. (See references 2–6.) These methods and ongoing efforts are encouraging developments for constructing more durable PT bridges. More time is needed to uncover pros and cons due to the limited experience with the new methods, but the bridge community has been moving forward in a positive direction.

Similarly, some strand materials possessing higher corrosion resistance than the conventional bare strand need consideration because they can tolerate potential problems stemming from defective grout materials and other construction-related deficiencies. The FHWA report covers several laboratory studies conducted more than ten yr ago at The University of Texas at Austin and Georgia Institute of Technology related to the corrosion resistance of different strand materials and currently available products in the U.S. market. (See references 1, 7–12.)

While corrosion-resistant strand materials are not common in U.S. bridges, several corrosion-resistant reinforcing bars, such as several grades of solid stainless steel, hot-dip galvanized steel, and epoxy-coated steel, have been widely used in ordinary reinforced concrete structures, especially bridge decks in northern States, over several decades. Despite higher material costs associated with using more corrosion-resistant rebars than conventional black rebars, the bridge community recognizes that the benefits outweigh the upfront costs. Similarly, by using alternative strand materials with better corrosion resistance in PT bridges, many problems, including temporary bridge closures,

U.S. Department of Transportation
Federal Highway Administration

Turner-Fairbank Highway Research Center

Research, Development, and Technology
Turner-Fairbank Highway Research Center
6300 Georgetown Pike
McLean, VA 22101-2296

https://highways.dot.gov/research

high repair and rehabilitation costs, and public safety risks due to unexpected tendon failures from corrosion, can be eliminated or significantly reduced.

Recognizing the need for an independent study with the help of the latest evaluation techniques, the FHWA Coatings and Corrosion Laboratory launched an in-house study to quantify the corrosion resistance of four metallic strand materials available in the current U.S. market that can be used in the new construction of PT bridges. The goal was to provide the bridge community with the latest information about the corrosion properties of alternative metallic strand materials that may promote more usage. The laboratory experiments were subjected to accelerated corrosion for 5 mo.

EXPERIMENTAL PROCEDURE

Strand Materials

In this study, four types of metallic seven-wire strands were acquired from two suppliers. These included a hot-dip galvanized strand (H), a flow-filled epoxy-coated strand with no grit (E), a grade 2205 duplex solid stainless-steel strand (S), and a new type of zinc/aluminum alloy-coated strand (Z). The zinc/aluminum alloy-coated strand has been available for nonbridge applications. With the conventional bare strand (B) as control, the research team compared four materials' corrosion characteristics under an accelerated corrosion testing program.

Figure 1 shows eight encapsulated specimens that were made with five strand materials. The research team arranged the specimens in a plastic mold before encapsulating them in fresh grout.

Conventional Bare Strand (B)

The 0.6-inch (15.2-mm) seven-wire B served as the control. The researchers used a low relaxation, grade 270 strand meeting the ASTM International (ASTM) A416/A416M specification.[13]

Hot-Dip Galvanized Strand (H)

The study used a 0.6-inch (15.2-mm) H seven-wire strand meeting the requirements of ASTM A475.[14] The FHWA Technical Advisory 5140.25 warning about the possibility of a loss of ductility in this type of strand due to hydrogen embrittlement (HE) was rescinded in January 2020.[15]

Zn/Al Coated Strand (Z)

The Z used was a 0.5-inch (12.7-mm) seven-wire strand coated with 95 percent zinc and 5 percent aluminum alloy.[16] Although this strand was produced for nonprestressed concrete applications, the researchers included it in the study to see how the new zinc alloy coating performs against the traditional H strand.

Figure 1. Photo. Five types of metallic seven-wire strand materials.

Source: FHWA.
HD, ZD, and ED = intentionally damaged H, Z, E, respectively.

Filled Epoxy-Coated Strand with No Grit (E)

The acquired E was manufactured with the 0.6-inch (15.2-mm) seven-wire strand meeting the ASTM A416/A416M requirements after going through mechanical cleaning and preheating followed by coating using the electrostatic spray method according to the ASTM A882/A882M.[13,17] The finished coating thickness can range from 15 to 45 mils (0.38–1.14 mm).[18]

Epoxy-coated strands were previously available in two configurations: conventional or filled strands. The conventional configuration is produced by spraying an epoxy coating around its exterior circumference. The filled configuration is made by spraying the coating after spreading seven wires apart so that interstices formed by the individual wires are filled with the plastic-state epoxy coating. Only E is available at present, either with a smooth surface or with grit particles embedded in the coating surface.[18] Figure 2 shows the cross-section of the filled epoxy-coated strand with no grit (see figure 2-A) and the conventional B containing empty interstices (see figure 2-B). The latter allows water to travel through the empty interstices. The filled interstices should hinder potential crevice corrosion originating from the interstices.

Grade 2205 Duplex Stainless Steel Strand (S)

The study used grade 2205 duplex 0.6-inch (15.2-mm) seven-wire solid stainless-steel strand meeting the requirements of grade 240 ASTM A1114/A1114M.[19]

ACCELERATED CORROSION TESTING

The study used accelerated corrosion testing consisting of three exposure conditions for up to 155 d to understand the corrosion characteristics of four metallic strand materials with respect to the B strand.

Figure 2. Photos. Cross-sectional views of two types of seven-wire strand materials.[1]

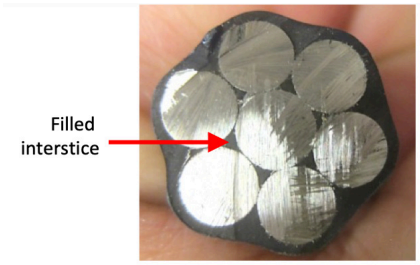

A. Filled epoxy-coated strand with no grit (E).

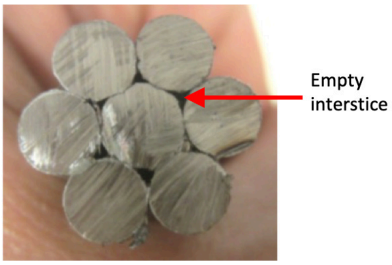

B. Conventional bare strand (B).

Source: FHWA.

Based on previous experience using accelerating corrosion testing methodologies, the researchers fabricated and tested three types of single-strand specimens in aqueous solutions and exposed the grout to chloride and sulfate ions. One of the study objectives was to quantify how many anions these strand materials could tolerate before initiating corrosion. Two chest freezers without electrical power were used to expose the specimens at the elevated temperature (104 °F (40 °C)). The target temperature inside each freezer was maintained using a heat lamp and a digital temperature controller.

Test Variables and Fabrication of Encapsulated Specimens

The following lists eight test variables that were incorporated into the experimental design:

- Strand materials (5): B, H, Z, E, and S.
- Strand types containing artificial coating defects (3): Damaged H (HD), damaged Z (ZD), and damaged E (ED).
- Testing medium (3): Aqueous solutions containing various anion concentrations, poor-quality grout (containing excessive water to create grout segregation), and good-quality grout (containing the maximum amount of water recommended by the grout manufacturer).
- Level of stress (1): No stress.
- Chloride concentration in aqueous solutions (6): 0, 0.08, 0.2, 0.4, 0.8, and 2.0 percent by weight of cement.
- Sulfate concentration in aqueous solutions (7): 0, 0.1, 0.2, 0.4, 0.8, 1.5, and 3.0 percent by weight of cement.
- The potential of hydrogen (pH) of aqueous test solutions (1): 7.
- Temperature (2): 77 °F (25 °C, ambient) for baseline data collection and 104 °F (40 °C) for accelerated corrosion testing.

All specimens used in this study were prepared by cutting unstressed individual strands into 8.5-inch long (216-mm long) segments. Then, one cut end of each segment was electrically connected to a 6-inch long (152-mm long) solid copper wire followed by encapsulating both cut ends with impermeable clear epoxy resin and 1.5-inch (38.1-mm) plastic caps. This step was critically important to ensure perfect isolation of the bare ends from the test environments. Figure 3 shows the schematics of the prepared specimens.

Figure 3. Illustration. Schematics of encapsulated specimens.

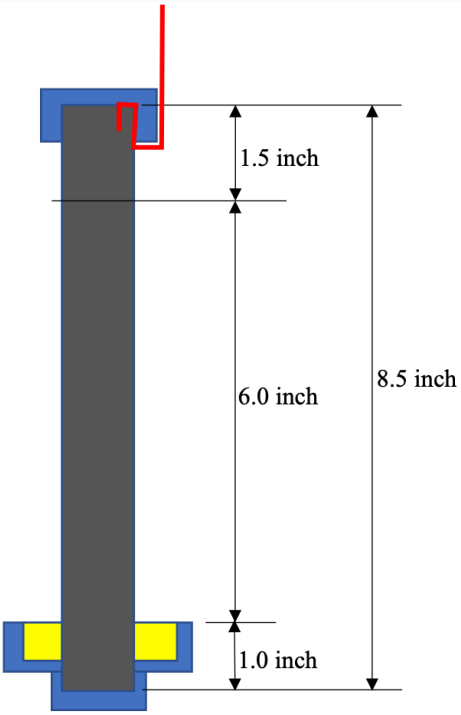

A. Strand type B, S, and all damage-free E, H, Z.

Source: FHWA.

Figure 3. Illustration. Schematics of encapsulated specimens. (Continued)

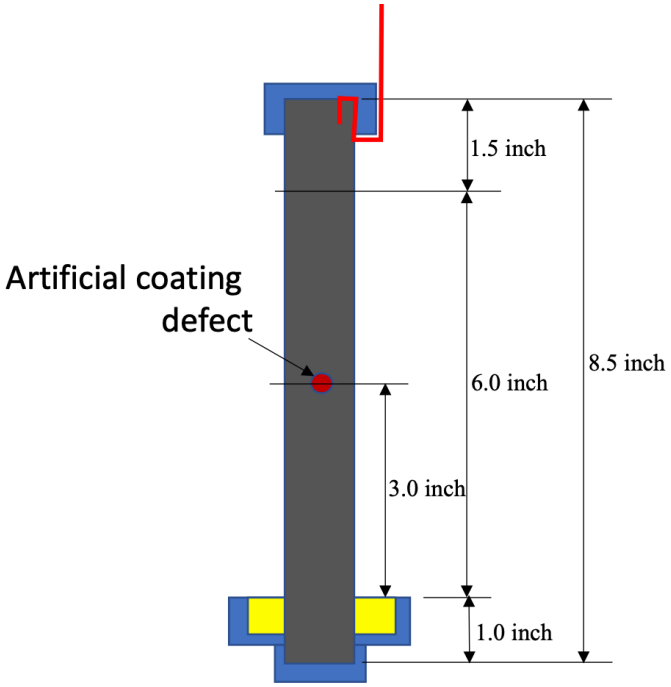

B. Strand type E, H, Z containing coating defects.

Source: FHWA.

Twenty-five percent of the coated strand specimens (H, Z, and E) were introduced with artificial coating defects using a hacksaw to simulate mechanical damage that may occur in the field. To ensure the initial defect-free condition of every E specimen, the researchers inspected the as-received coating condition with a low-voltage holiday detector.

Testing in Aqueous Solutions

The first experiment used 220 specimens (4 specimens/strand type × 5 strand types × 11 test conditions). The specimens were tested in large test cells made with chemical-resistant plastic containers filled with the aqueous test solutions.

Researchers employed a conventional three-electrode configuration using the strand as the working electrode (WE), a half-cylindrical shaped stainless-steel mesh as the counter electrode (CE), and a silver/silver chloride (Ag/AgCl) reference electrode (RE). These electrodes were immersed in the aqueous solution, which served as the electrolyte.

Figure 4 shows a schematic of the test cell. Each test cell accommodated four same-type strand specimens. In each test cell prepared for the coated specimens (H, Z, E), the first three specimens (WE no. 1–WE no. 3) had no coating damage, and the fourth one (WE no. 4) had a single defect at the middepth.

Figure 4. Illustration. Schematic of aqueous solution testing setup.

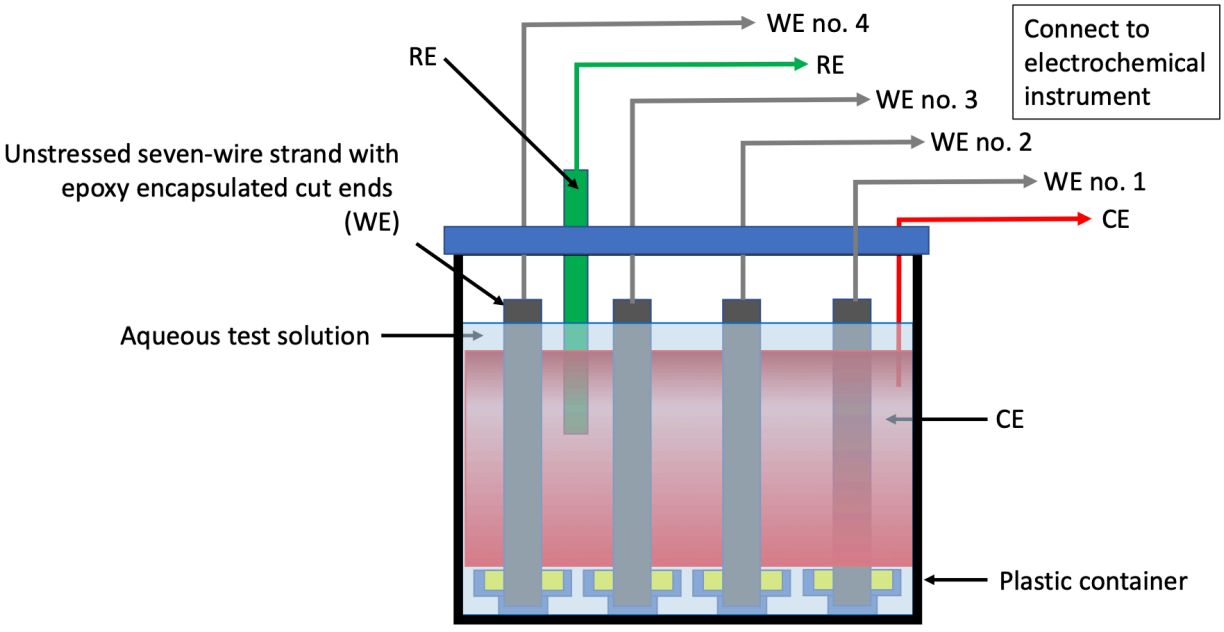

Source: FHWA.

As listed in table 1, aqueous solutions were made with pH 7 deionized (DI) water containing five chloride concentrations (0.08, 0.2, 0.4, 0.8, and 2.0 percent by weight of cement) and five sulfate concentrations (0.1, 0.2, 0.4, 0.8, and 2.0 percent by weight of cement). From this point, all anion concentrations will be mentioned without the "by weight of cement" note. Anion-free DI water was also included as the control solution.

Prior to the aqueous solution testing, the research team immersed each specimen in simulated pore water (pH 13.6) for 7 d. This preconditioning step allowed a stable passive film to be formed on the strand surface, similar to the initial protection of actual strands in fresh grout. After preconditioning, researchers gently washed the specimens with tap water and immersed in DI water for 2 h. Finally, the specimens were placed in a test cell filled with a test solution. Upon observing their stable open-circuit potentials (OCPs) within 2 h, the baseline corrosion rates (CRs) and accompanying OCPs were measured by the linear polarization resistance (LPR) method at 77 °F (25 °C). For defect-free E specimens, baseline coating resistance (Rc) using the electrochemical impedance spectroscopy (EIS) method was measured with a wide range of frequency, from 100 kHz to 0.01 Hz, because the direct current (DC)-based LPR method cannot work through the high-impedance epoxy coating. The defect-free E specimens' OCPs could not be measured for the same reason.

Table 1. Test Matrix

Testing Medium	Specimen Type	Exposure Condition	Concentration of Anions* (percent)	Specimen Type**								Number of Specimens
				B	H	HD	Z	ZD	E	ED	S	
Aqueous solutions	Unstressed single strand	pH 7 aqueous solutions at 104 °F	0	4	3	1	3	1	3	1	4	20
			C = 0.08	4	3	1	3	1	3	1	4	20
			C = 0.2	4	3	1	3	1	3	1	4	20
			C = 0.4	4	3	1	3	1	3	1	4	20
			C = 0.8	4	3	1	3	1	3	1	4	20
			C = 2.0	4	3	1	3	1	3	1	4	20
			S = 0.1	4	3	1	3	1	3	1	4	20
			S = 0.2	4	3	1	3	1	3	1	4	4
			S = 0.4	4	3	1	3	1	3	1	4	4
			S = 0.8	4	3	1	3	1	3	1	4	4
			S = 2.0	4	3	1	3	1	3	1	4	4
	Number of specimens per strand type			**44**	**33**	**11**	**33**	**11**	**33**	**11**	**44**	**Subtotal = 220**
Covered with poor-quality grout	Unstressed single strand	Aqueous solutions at 104 °F	C = 0.4	3	3	3	3	3	3	3	3	24
			S = 0.4	3	3	3	3	3	3	3	3	24
	Number of specimens per strand type			**6**	**6**	**6**	**6**	**6**	**6**	**6**	**6**	**Subtotal = 48**
Covered with good-quality grout	Unstressed single strand	Ponding solutions at 104 °F	C = 0.4	3	3	3	3	3	3	3	3	24
			S = 0.4	3	3	3	3	3	3	3	3	24
	Number of specimens per strand type			**6**	**6**	**6**	**6**	**6**	**6**	**6**	**6**	**Subtotal = 48**
												Total = 316

*C = chloride ions; S = sulfate ions.

Upon completion of the baseline data collection, the test cells were transported to the freezers that were maintained at 104 °F. After 7 d, the final measurements of CRs and OCPs (or Rc for E and Rc/OCP for ED) were made at 104 °F (40 °C).

Testing in Poor-Quality Grout

As listed in table 1, the research team conducted the second experiment with 48-strand specimens wrapped with defective grout as shown in figure 5.

This type of poor-quality grout specimens was fabricated by wrapping a cylindrical-shaped grout layer over the encapsulated specimens shown in figure 3. A thin clear plastic sheet wrapped around the specimen served as a mold. Researchers created intentionally segregated, poor-quality grout by mixing a prepackaged grout product with excessive mixing water. As a result, randomly formed cracks and porous areas occurred in each specimen. The intention was to see how the specimens would respond to poor-quality grout. The only drawback of this method was the inability to introduce identical grout defects consistently to every specimen. The number of artificial coating defects on the damaged specimens also increased to two.

After a 14-d curing period, six groups of poor-quality grout specimens were assembled for immersion testing as shown in figure 4. Each group consisted of eight types of encapsulated specimens shown in figure 1. Then, the first three groups were placed into separate test cells and filled with the identical aqueous solution containing 0.4 percent chloride ions. Similarly, the remaining three groups were tested in the aqueous solution containing 0.4 percent sulfate ions.

After the baseline data (LPR/OCP and macrocell (galvanic) corrosion current (Imacro) for B, H, Z, and S specimens, Rc for E specimens, and Rc/OCP for damaged E specimens) were collected at 77 °F (25 °C), the specimens were transferred to the freezers and exposed to the elevated temperature. Multiple rounds of data collection were made periodically at 104 °F (40 °C) for 155 d.

Testing in Good-Quality Grout

As listed in table 1, the third and last experiment employed 48 specimens embedded in 6 good-quality grout slabs. Each slab contained eight encapsulated strand specimens. Figure 1 and figure 6 show the specimen arrangement before and after pouring fresh grout into a plastic mold, respectively.

The top and bottom grout covers were each approximately 0.5 inches (12.7 mm) thick. The number of artificial coating defects on the damaged specimens increased to three after observing no clear effect of coating defects

Figure 5. Photo. An encapsulated specimen wrapped in poor-quality grout.

Source: FHWA.

Figure 6. Photo. Eight encapsulated specimens buried in a good-quality grout slab.

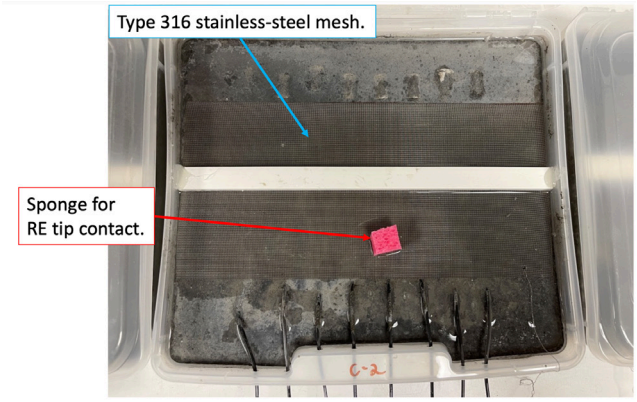

Source: FHWA.

in the previous experiments. The researchers made the good-quality grout with a prepackaged commercial product and the manufacturer's recommended water amount. Using good-quality grout produced no visible grout defects, and the researchers were able to investigate the corrosion performance of the strand materials in the good-quality grout.

After a 14-d curing period, the top surfaces of three slabs were covered with the aqueous solution containing 0.4 percent chloride ions and those of the remaining slabs with another aqueous solution containing 0.4 percent sulfate ions. Figure 6 shows a stainless-steel mesh placed on top of each slab as the CE in the ponding solution. A small piece of sponge was placed on top of the CE to protect the RE's tip from contacting the CE during data collection.

Like the second experiment, after the stable OCPs were observed, followed by the baseline data collected at 77 °F (25 °C), researchers transferred the slabs to the freezers and exposed the slabs to the elevated temperature. Multiple rounds of data collection were made periodically at 104 °F (40 °C) for 150 d.

Electrochemical Testing

Researchers employed conventional DC corrosion testing methods LPR, OCP, and Imacro for the specimens, except for the E and ED specimens.

Linear Polarization Resistance Measurement

The LPR measurements were made to quantify the corrosion resistance of the specimens exposed to different conditions in terms of polarization resistance (PR) and OCP using a three-electrode (i.e., WE, CE, and RE) configuration.

A potentiostat applied a small increment of direct voltage between the WE and CE, from −10 mV with respect to the specimen's OCP (i.e., corrosion potential (E_{corr})) to +10 mV, at a scan rate of 0.5 mV/s and a sampling period of 2 s. This process is called polarization. The corresponding current output data in response to each polarized potential step were recorded. Subsequently, the slope of the linear region found between the potential and the current data points, as shown in figure 7, determined the PR (=ΔE/ΔI) of the specimen.

Figure 7. Illustration. LPR measurement.[20]

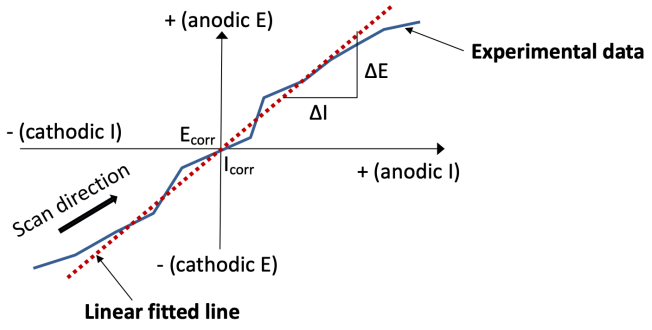

Source: FHWA.
E_{corr} = Open-circuit potential (corrosion potential); I_{corr} = Corrosion current; ΔE = voltage difference; ΔI = current difference.

Researchers applied experimentally determined PR to calculate the instantaneous CR at the time of measurement in terms of uniform penetration rate. Since most of the strand materials employed in this study were alloy-based materials or coated, researchers directly used PR—inversely proportional to CR and a kinetic aspect of the corrosion—to compare the corrosion intensities of the different strand materials exposed to an identical condition. Furthermore, surface areas were not used to calculate normalized PR values for this analysis.

Open Circuit Potential Measurement

The OCP indicates the thermodynamic aspect of corrosion. During all PR measurements, OCP was determined during the data collection and analysis work (see figure 7).

Macrocell Corrosion Current Measurement

Researchers collected the Imacro by measuring the galvanic current flow between each specimen (WE) in the grout and the CE at every second for 120 s. The last Imacro value of a specimen was considered its nominal Imacro. Typically, the Imacro gradually decreases with time, and more active materials produce higher Imacro. Figure 8 shows Imacro data obtained from four strand materials (B, H, Z, and S) that were exposed to 0.4 percent chloride in poor-quality grout for 155 d.

EIS

EIS is an advanced experimental technique that determines various electrochemical parameters nondestructively in many fields. For coating applications, EIS is proven to be the most effective tool to investigate coating properties and their changes with time: Rc and coating capacitance; charge transfer resistance (Rct) and double-layer capacitance at the coating/metal substrate; and diffusion-related phenomenon at the coating and interface. The drawbacks include a sophisticated instrument with a special experimental setup and much experience to analyze the EIS data correctly.

Figure 8. Graph. Examples of Imacro data.

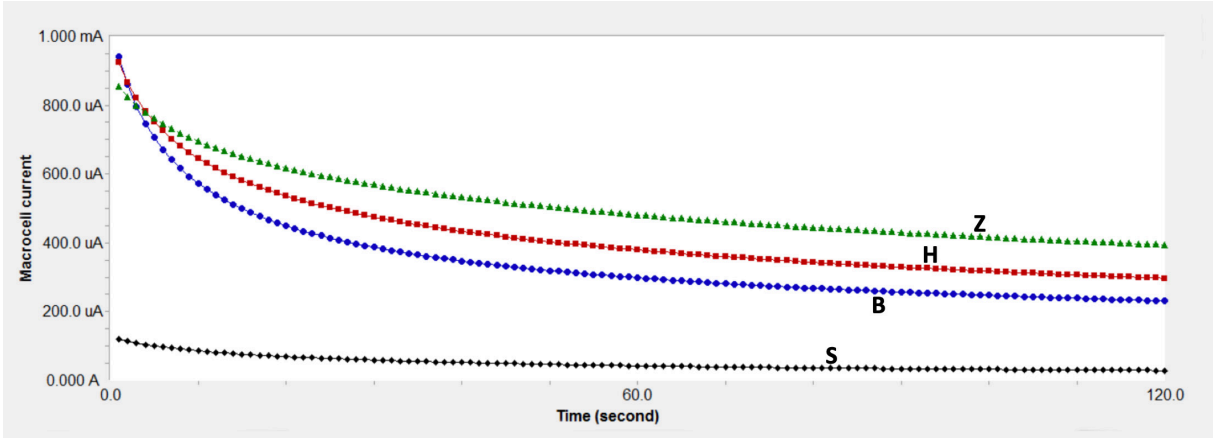

Source: FHWA.

In this study, whenever the DC testing was performed with the other type specimens, the EIS data from each E specimen were also collected from 100,000 to 0.01 Hz. In one decade of frequency, 10 data points were scanned with a sinusoidal amplitude of 200 mV. The collected EIS data were analyzed using two equivalent circuit (EC) models that are well established for coated steel. This report presents Rc data only as the primary protective coating properties.

Figure 9 shows EIS data obtained from a defect-free E specimen after 150 d in good-quality grout exposed to 0.4 percent chloride ions: Bode magnitude and phase angle plots in figure 9-A and a Nyquist plot in figure 9-B.

Because the defect-free specimen did not have coating defects, a purely capacitive behavior is present in the EIS response:

- A straight line in the Bode magnitude plot (in log scale).
- Near −90-degree phase angles in the Bode phase angle plot.
- A steep arc segment in the Nyquist plot.

Figure 10 shows an EC model used to fit the data shown in figure 9.

Figure 9. Graphs. Purely capacitive response from an E specimen.

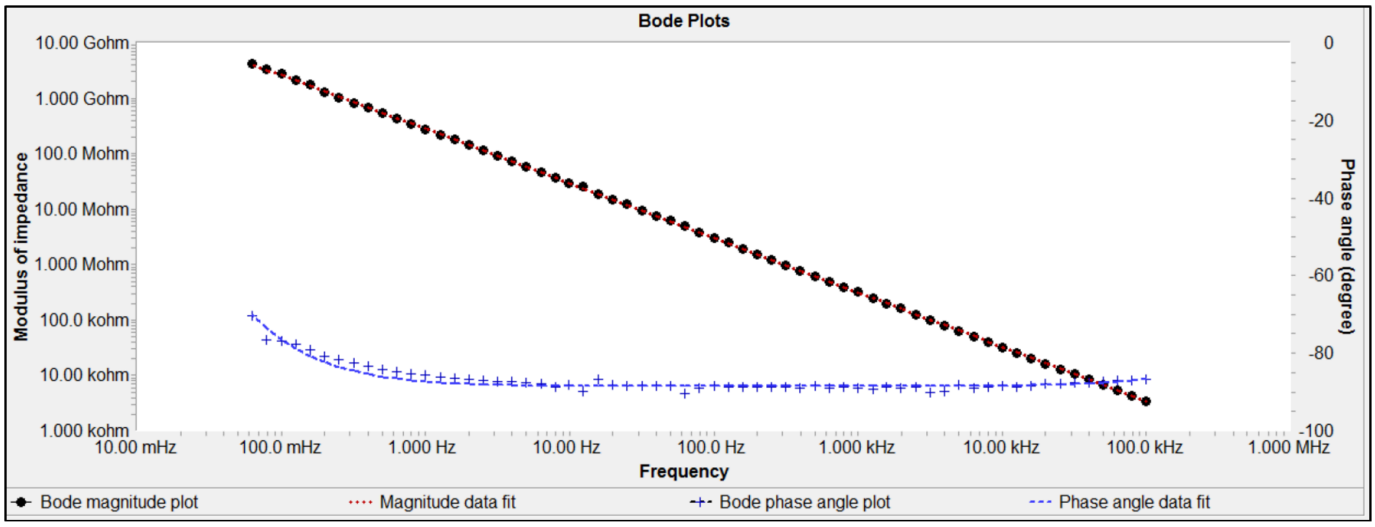

A. Bode plots.

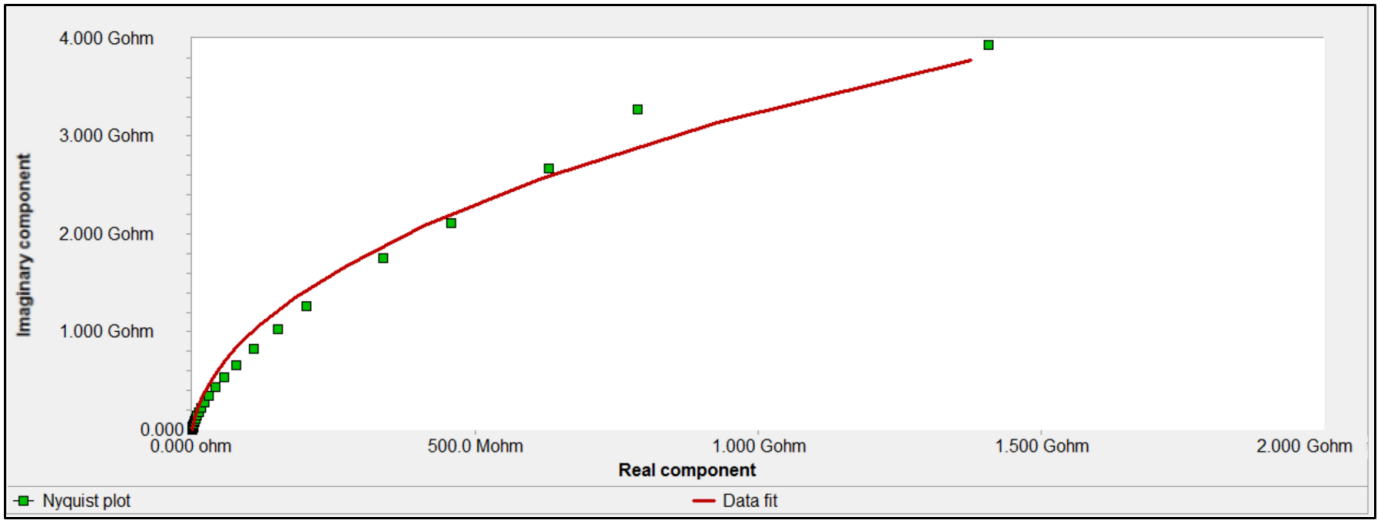

B. Nyquist plot.

Source: FHWA.

Figure 10. Illustration. An equivalent circuit model for defect-free E specimens.

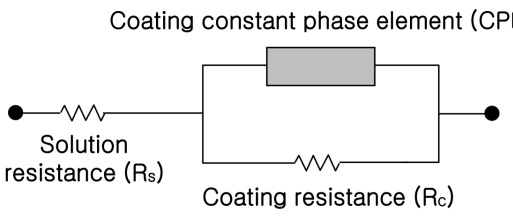

Source: FHWA.

Most of the EIS data obtained from real specimens and structures exhibit nonreal responses apart from the actual capacitors. Several circuit elements called constant phase elements (CPEs) are used to fit the experimental data and produce theoretical pseudo-capacitance values. The EC model in figure 10 contains a CPE for coating (CPEc). The superimposed fit results over the EIS data points in figure 9 show that both experimental and theoretical impedance data agreed well.

Figure 11 shows other EIS data obtained from an ED specimen after 150 d in good-quality grout exposed to 0.4 percent chloride ions: Bode magnitude phase angle plots in figure 11-A and a Nyquist plot in figure 11-B.

Figure 11. Graphs. EIS response from an ED specimen.

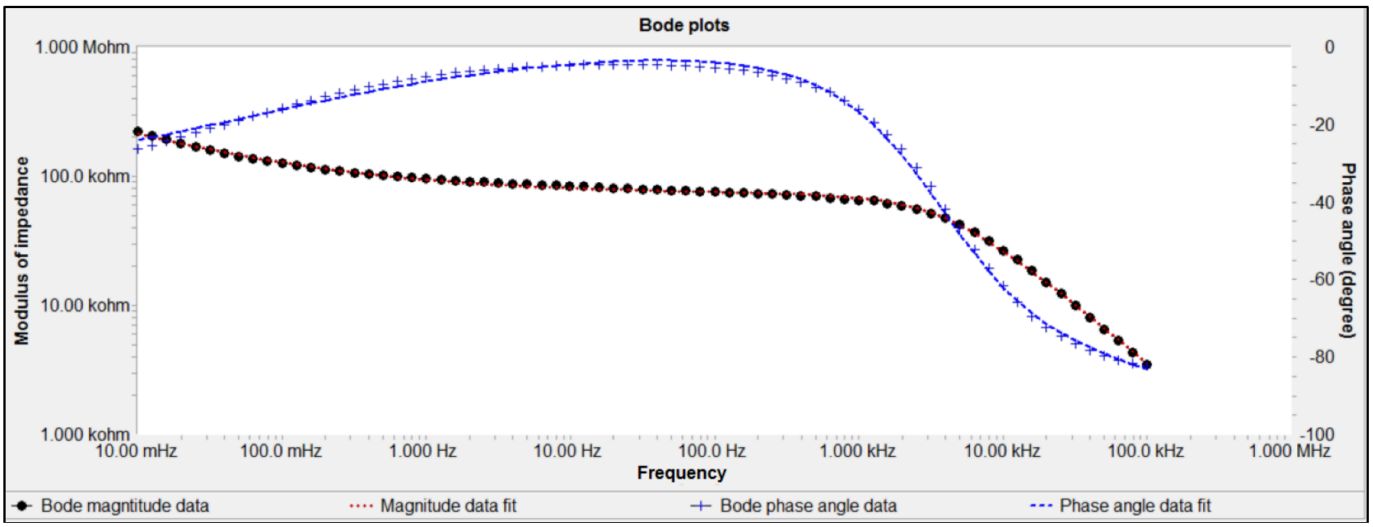

A. Bode plots.

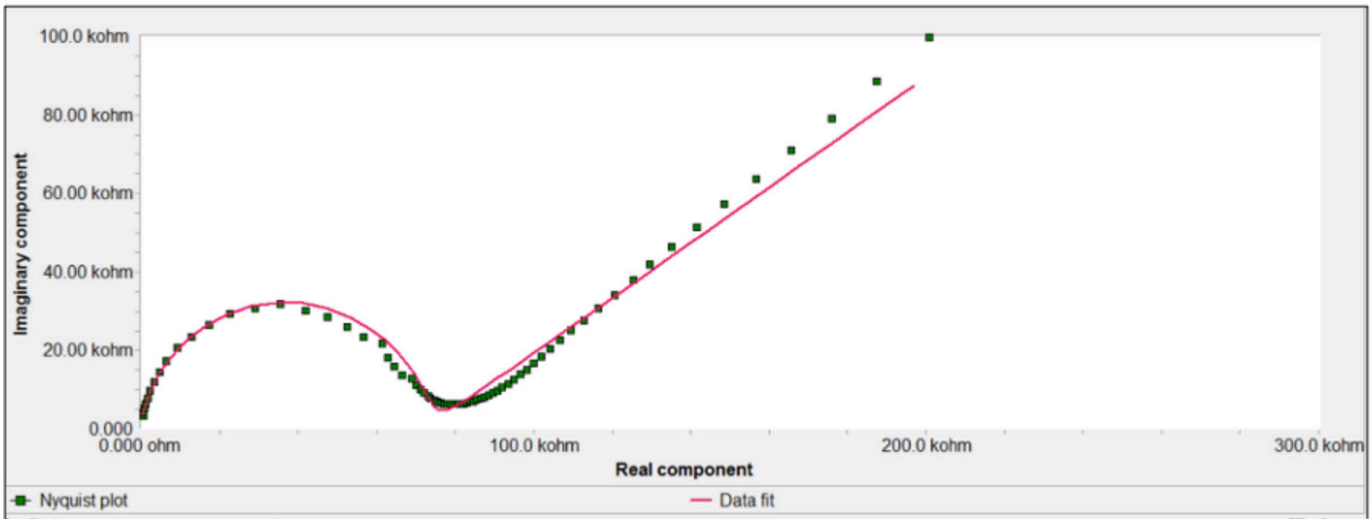

B. Nyquist plot.

Source: FHWA.

Because this specimen contained three artificial coating defects, different EIS responses were observed from those shown in figure 9:

- An inclined line section followed by a somewhat plateau region in the Bode magnitude plot (in log scale).
- A wide fluctuation from near −90 to 0-degree phase angles in the Bode phase angle plot.
- A depressed semicircle followed by a small arc portion of the second semicircle.

Figure 12 shows another EC model that can fit the data shown in figure 11. Because of the coating defects, the EC model added two more elements (Rct and double layer CPE) to account for the exposed bare area-related response. The superimposed fit results over the EIS data points in figure 11 look reasonably good.

TEST RESULTS AND DISCUSSION

This section presents the representative test results based on the representative data trends obtained from the comprehensive analysis work.

Polarization Resistance and Open Circuit Potential Data Classified By Exposure Conditions

The initial analysis of the aqueous solution data indicated that mean PR and OCP values of H and Z data collected from three defect-free specimens were not much different

Figure 12. Illustration. An equivalent circuit model for damaged ED specimens.

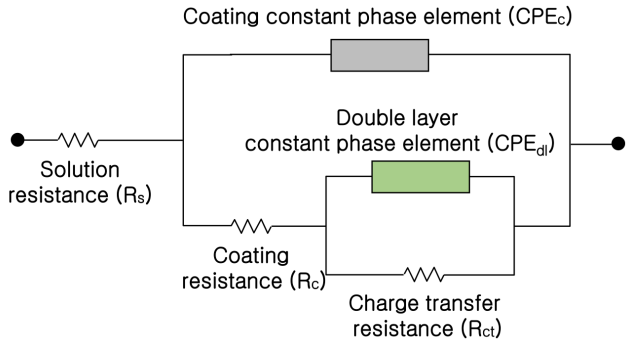

Source: FHWA.

from those after adding one more data point from the fourth specimen containing artificial damage. In other words, the impact of introducing small damage was not significant. Therefore, all four data points per specimen type were used to calculate their mean values throughout the analysis of aqueous solution data.

Figure 13 and figure 14 show the mean PR data and the matching mean OCP data, respectively, obtained from B, H, Z, and S specimens exposed to aqueous solutions containing chloride ions.

As expected, the most corrosion-resistant S specimens exhibited the highest PRs (i.e., the lowest CR) and the most positive OCPs (i.e., the least tendency for corrosion).

Figure 13. Graph. Mean PR data from B, H, Z, and S specimens exposed to aqueous solutions containing chloride ions.

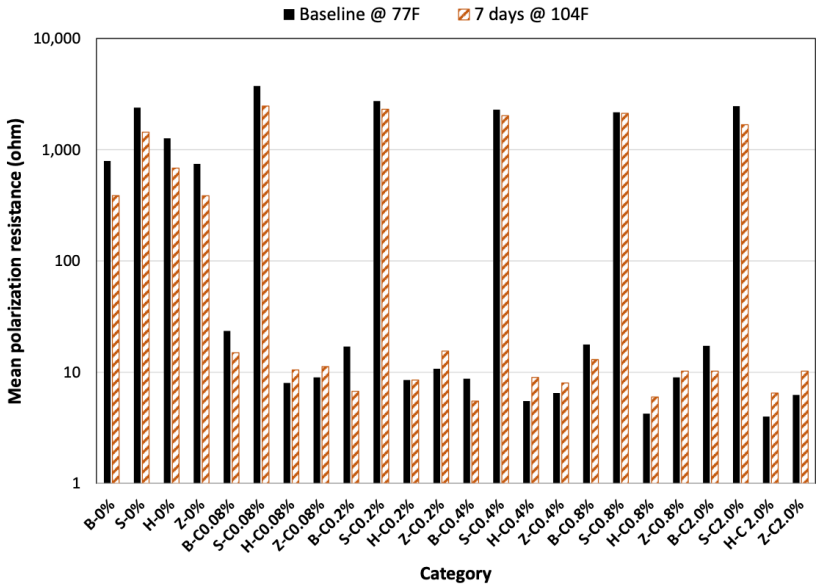

Source: FHWA.

Figure 14. Graph. Mean OCP data from B, H, Z, and S specimens exposed to aqueous solutions containing chloride ions.

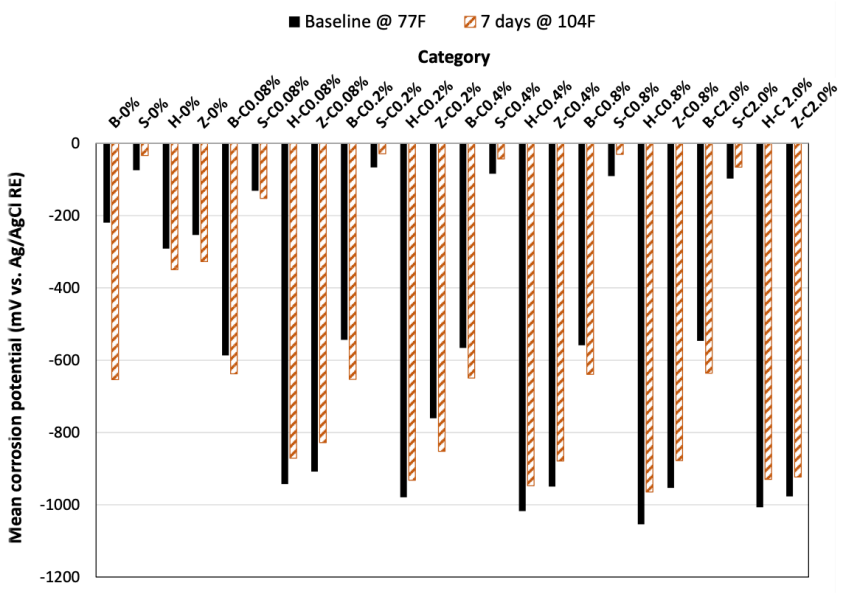

Source: FHWA.

The chloride-free condition also yielded high PRs and more positive OCPs, regardless of specimen type, compared to the chloride-contaminated conditions. The effects of chloride concentration level and a temperature change from 77 to 104 °F (25 to 40 °C) were not significantly noticeable. The PR and OCP data pertaining to the sulfate ions showed similar trends.

However, mean OCP values of H and Z specimens were quite negative (i.e., below −900 mV versus Ag/AgCl RE ($mV_{Ag/AgCl}$)) in all chloride environments due to the presence of zinc coating. HE may be possible in such a negative potential region via the water dissociation process—water molecules and electrons break into hydrogen gas and hydroxyl ions as a cathodic reaction on the metal surface—in neutral and high-pH environments. HE is one form of environmentally induced cracking phenomenon. The atomic hydrogen can enter the crystal lattice of certain metals and alloys and cause brittle cracking upon losing ductility. Detrimental effects of the HE includes unexpected brittle fractures of the stressed structural members like PT strands. Therefore, a follow-up study is recommended to investigate the possibility of HE that may occur in the fully stressed H strands surrounded by fresh grout with and without anions.

Figure 15 and figure 16 show the cumulative mean values with the time of the PR and OCP data, respectively, from B, H, HD, Z, ZD, and S specimens embedded in good-quality grout exposed to 0.4 percent chloride concentration.

By employing a cumulative mean approach, data variations at different times among the same specimen type were reduced such that relatively smooth data trends could be seen. Since an equal number of specimens (triplicate) for defect-free and damaged specimens per specimen type were tested, each group was treated separately.

In good-quality grout, the mean PR and OCP values of each group changed with time initially and stabilized after 50 d. All of the values remained virtually unchanged until the experiment was terminated at 150 d. The unchanging values indicate that chloride ions did not reach the strand specimens. As observed in figure 13 and figure 14, S specimens exhibited the highest PR and the most positive OCP among the six specimen types. The PR and OCP values of the S specimens were getting close to the others with time, though. Again, H and Z specimens remained below −900 $mV_{Ag/AgCl}$ in the good-quality grout throughout the experiment, regardless of their surface condition (defect-free versus damaged). Initial mean OCPs in fresh grout were below −1,000 $mV_{Ag/AgCl}$.

The data from the good-quality grout exposed to sulfate ions and those from the poor-quality grout specimens exhibited similar data trends.

Figure 15. Graph. Cumulative mean PR data from B, H, HD, Z, ZD, and S specimens embedded in good-quality grout exposed to 0.4 percent chloride ions.

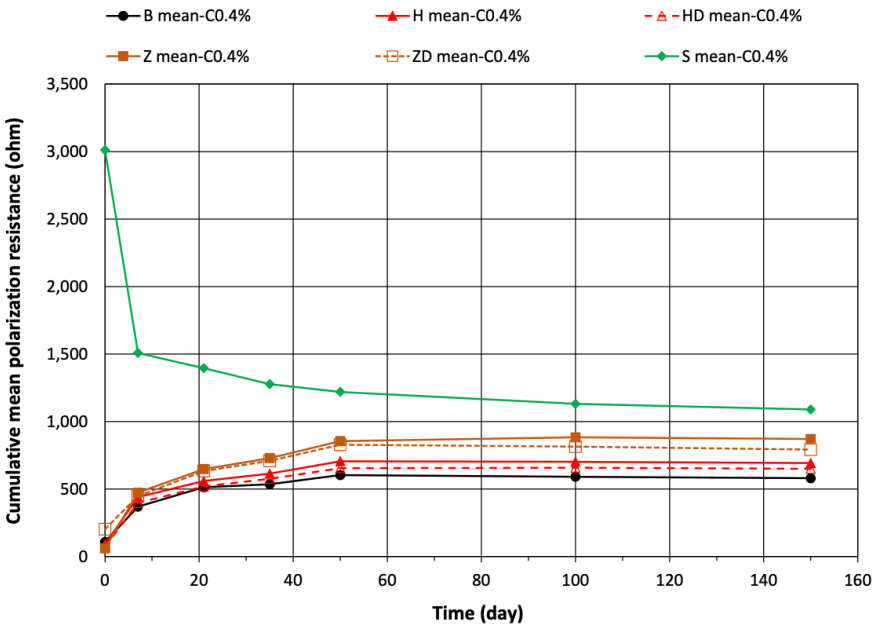

Source: FHWA.

Figure 16. Graph. Cumulative mean OCP data from B, H, HD, Z, ZD, and S specimens embedded in good-quality grout exposed to 0.4 percent chloride ions.

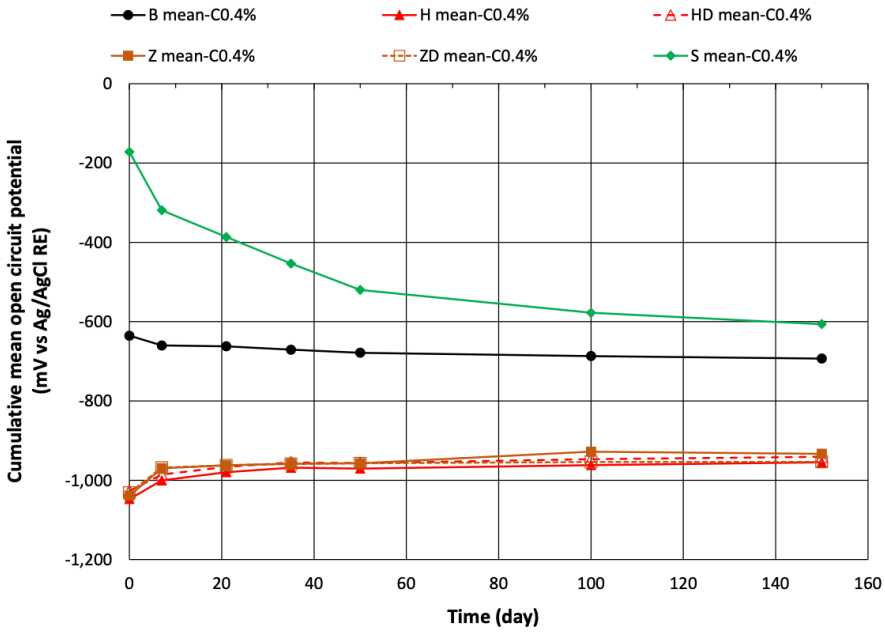

Source: FHWA.

Macrocell Corrosion Current Data

Figure 17 shows the cumulative mean values of Imacro data with the time from B, H, HD, Z, ZD, and S specimens embedded in good-quality grout exposed to 0.4 percent chloride concentration. Again, defect-free and damaged specimens within the same specimen type were treated separately.

Like the mean PR data (figure 15) and mean OCP data (figure 16), the mean Imacro values of each data group were initially the highest in good-quality grout and then stabilized after 50 d and remained unchanged until the experiment was terminated at 150 d. Since Imacro tends to be more sensitive to chloride ions, it was likely that chloride ions did not reach the specimens through the 0.5-inch (12.7-mm) grout cover.

As opposite trends to the mean PR and OCP data, S specimens exhibited the lowest Imacro (in other words, the lowest CR), and H specimens exhibited the highest Imacro (the highest CR).

Furthermore, the damaged specimens (HD and ZD) produced almost identical mean Imacro to those of the intact counterparts (H and Z), regardless of exposure duration. Also, the data trends related to the Z and ZD specimens followed the H and HD specimens with a reduced Imacro of about 200 µA. This means that H and HD specimens were more active than Z and ZD specimens.

The data from the good-quality grout exposed to sulfate ions and those from the poor-quality grout specimens exhibited similar data trends.

Coating Resistance Data

Figure 18 shows the cumulative mean values of Rc data with time determined from E and ED specimens embedded in good-quality grout exposed to 0.4 percent chloride concentration and 0.4 percent sulfate concentration.

Since there was an equal number of specimens (triplicate) for defect-free and damaged E specimens, they were treated separately. Figure 18 shows that the introduction of three artificial coating defects reduced the mean Rc values from more than several 10^{11} ohms to nearly 10^{4} ohms. Most ED specimens in aqueous solutions also exhibited Rc values between 100 and 10,000 ohms. Furthermore, OCP could not be measured from E specimens due to their perfect isolation from the electrolyte, whereas OCP values of the ED specimens were around −600 $mV_{Ag/AgCl}$, independent of anion concentration.

Figure 17. Graph. Cumulative mean Imacro data from B, H, HD, Z, ZD, and S specimens embedded in good-quality grout exposed to 0.4 percent chloride ions.

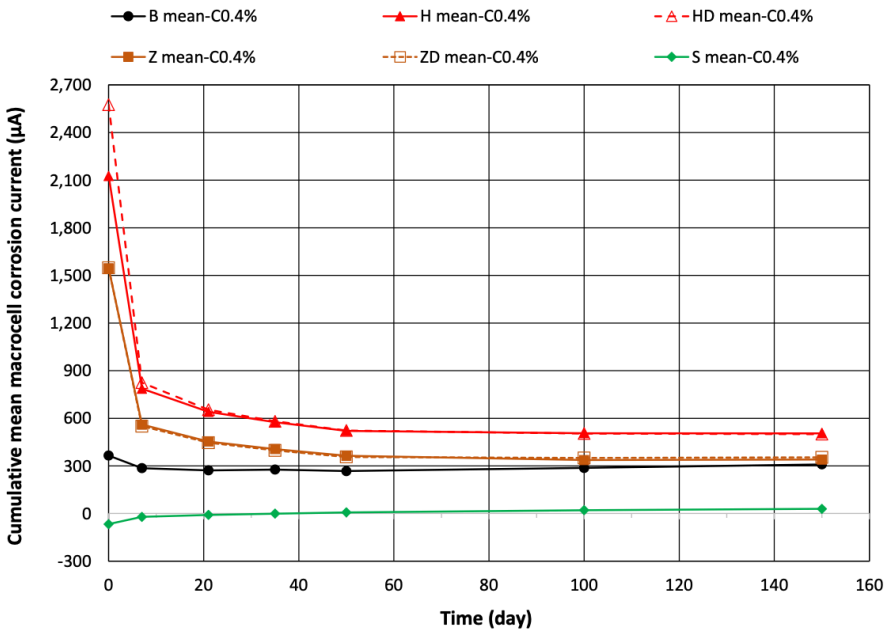

Source: FHWA.

Figure 18. Graph. Cumulative mean Rc data from E and ED specimens embedded in good-quality grout exposed to 0.4 percent chloride and sulfate ions.

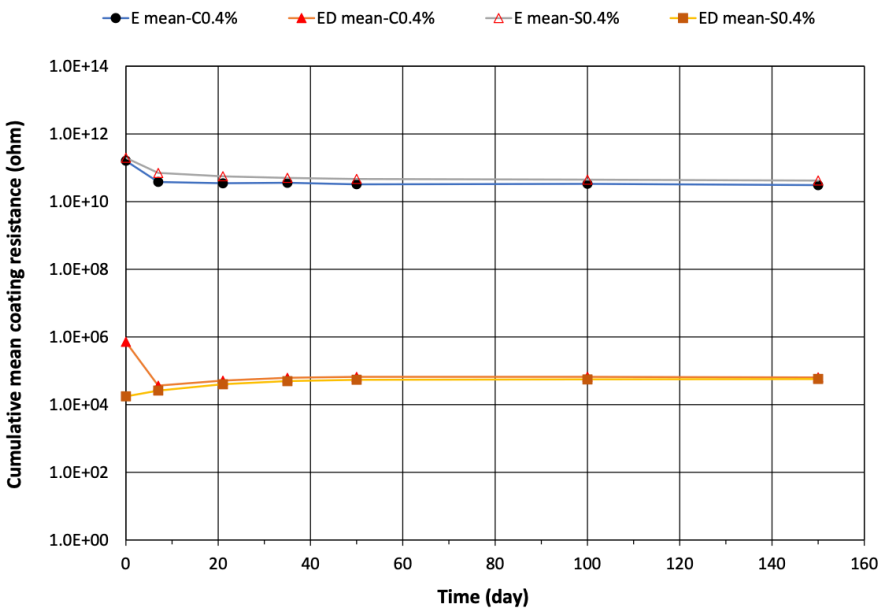

Source: FHWA.

Once mean Rc values were stabilized in the good-quality grout within 20 d, they did not change until the experiment was terminated at 150 d. The Rc data obtained from the poor-quality grout specimens showed similar trends.

Contrary to the insignificant changes by introducing artificial damage to the H and Z specimens protected by metallic coatings, a drastic Rc reduction of E specimens—more than six orders of magnitude—signifies the importance of maintaining coating integrity throughout the entire construction process. Good construction practice can maintain coating integrity with the help of stringent quality control and quality assurance measures and by creating careful steps to install flawless electrically isolated tendons.

CONCLUSIONS AND RECOMMENDED FOLLOW-UP STUDIES

The data collected during the 5 mo of accelerated corrosion testing suggests that this study might be too short to lead to solid conclusions based on comparative corrosion performance data and whole-life cost analysis among the tested materials. However, this document still presents important research outcomes that provide new quantitative information about these strand materials' corrosion characteristics. The following are the conclusions and recommendations:

1. The experimental data verified that the B strand exhibited the lowest corrosion resistance among the five strand materials employed in this study. On the other hand, the grade 2205 duplex S strand performed very well, evidenced by the most positive OCP (or corrosion potential, i.e., least corrosion tendency), the highest PR (i.e., the lowest CR), and the lowest macrocell (galvanic) corrosion current (Imacro, the lowest corrosion intensity similar to CR) in every testing condition.

2. The H strand was the most active (thermodynamically corrosion susceptible) material, evidenced by very negative OCPs (the highest corrosion tendency), the least PR (the highest CR), and the largest Imacro (the highest corrosion intensity) among the five strand materials tested in this study. Also, H's corrosion performance indicators were not influenced by the small coating defects introduced in this study. Perhaps a higher damage level may be needed to see discernible results. Another zinc coating-based Z strand also exhibited closely similar corrosion behaviors as the H strand. It is unknown how long the zinc layers on the H and Z specimens will provide sufficient corrosion protection to the underlying steel in various service conditions. Judging from the observed very negative OCP values between −900 and more negative than −1,000 mV versus silver/silver chloride reference electrode during this short-term study, the possibility of HE leading to brittle fracture in the H (and also Z) strand cannot be ruled out conclusively.

3. The main corrosion performance indicator of the E strand was different from the other materials: Rc determined with an alternating current-based technique (EIS), instead of direct current-based PR/OCP/Imacro techniques. Another impedance parameter—Rct at the coating defects—was related to defect size and testing medium, not the coating itself. Although the testing duration was too short to be resolutely conclusive, the E strand showed very encouraging performance due to its high-quality electrical insulation barrier offered by the filled-in epoxy coating. While potential long-term corrosion can be developed at the coating damage and in the anchorage zone where the coating cannot protect the wedged area, use of this material without the ducts and grout to replace the grouted external tendons inside the box girders is worth exploring. If this approach is proven successful through some field trials like more than 300 bridges containing different types of the E strands in Japan, many problems associated with inspections and other maintenance activities, including tendon replacement, can be solved, or at least reduced.[18]

4. The susceptibility of the HE should be investigated thoroughly using realistically constructed mockup tendons containing fully stressed H strands exposed to uncarbonated grout.

5. The minimal corrosion risk of the E strand containing various coating conditions (i.e., coating defects) and at the anchorage zone should be confirmed. In addition, large-scale field trials replacing the grouted external tendon with bare E-strand systems would be a worthy effort to improve the inspectability and durability of PT bridges.

REFERENCES

1. Lee, S-K. 2022. *Corrosion-Induced Durability Issues and Maintenance Strategies for Post-Tensioned Concrete Bridges*. Report No. FHWA-HRT-22-090. Washington, DC: Federal Highway Administration. https://highways.dot.gov/research/publications/infrastructure/FHWA-HRT-22-090, last accessed October 23, 2022.

2. Post-Tensioning Institute. 2015. *Selection of Filler Material for Multistrand PT Tendons*. PTI Technical Note 19. Farmington Hills, MI: Post-Tensioning Institute. https://www.post-tensioning.org/Portals/13/Files/Pdfs/Education/Technical%20Note_19.pdf, last accessed April 23, 2024.

3. Hamilton, H. R., and J. A. Rice. 2017. *Replaceable Unbonded Tendons for Post-Tensioned Bridges*. Report No. BDV31-977-15. Gainesville, FL: University of Florida.

4. Whitmore, D. W., and M. R. Beaudette. 2016. "Impregnation of Post-Tensioning Tendons." *Aspire Magazine* Winter 2016: 36–37. Chicago, IL: Precast/Prestressed Concrete Institute.

5. Angst, U., and M. Büchler. 2021. *State-Of-The-Practice Report: Monitorable Post-Tensioning Systems*. Report No. FHWA-HIF-19-094. Washington, DC: Federal Highway Administration. https://www.fhwa.dot.gov/bridge/concrete/hif19094.pdf, last assessed November 2, 2022.

6. FHWA. 2021. *Development of Reference Criteria for Electrically Isolated Post-Tensioning Tendons in U.S. Bridge Applications*. Publication No. FHWA-HIF-20-042. Washington, DC: Federal Highway Administration. https://www.fhwa.dot.gov/bridge/concrete/hif20042.pdf, last assessed November 2, 2022.

7. Kilduff, A. L., K. L. Moyer, G. E. McCool, M. E. Ahern, and J. E. Breen. 2013. *Corrosion Resistance Recommendations from Long-Term Exposure Testing of Post-Tensioning Systems*. Report No. FHWA/TX-13/0-4562-5F. Austin, TX: The University of Texas at Austin.

8. Kalina, R. D. 2009. "Comparative Study of the Corrosion Resistance of Different Prestressing Strand Types for Use in Post-Tensioning of Bridges." Master's thesis. University of Texas at Austin. https://fsel.engr.utexas.edu/pdfs/FINAL.pdf, last accessed April 23, 2024.

9. Mac Lean, S. 2008. "Comparison of the Corrosion Resistance of New and Innovative Prestressing Strand Types Used in Post-Tensioning of Bridges." Master's thesis. University of Texas at Austin. https://fsel.engr.utexas.edu/pdfs/Mac%20Lean,S.pdf, last accessed April 23, 2024.

10. McCool, G. E. 2010. "Evaluation of Corrosion Resistance of New and Upcoming Post-Tensioning Materials After Long-Term Exposure Testing." Master's thesis. University of Texas at Austin. https://repositories.lib.utexas.edu/items/1156db15-51a2-4628-961d-a2f149b7945f, last accessed April 23, 2024.

11. Moyer, K. L. 2012. "Assessment of Long-Term Corrosion Resistance of Recently Developed Post-Tensioning Components." Master's thesis. University of Texas at Austin. https://fsel.engr.utexas.edu/pdfs/MOYER-THESIS.pdf, last accessed April 23, 2024.

12. Moser, R. D. 2011. "High-Strength Stainless Steels for Corrosion Mitigation in Prestressed Concrete: Development and Evaluation." Ph.D. dissertation. Georgia Institute of Technology.

13. ASTM. 2018. *Standard Specification for Low-Relaxation, Seven-Wire Steel Strand for Prestressed Concrete*. ASTM A416/A416M-18. Volume 04.02. West Conshohocken, PA: ASTM.

14. ASTM. 2014. *Standard Specification for Zinc-Coated Steel Wire Strand*. ASTM A475-03. West Conshohocken, PA: ASTM International.

15. FHWA. 2020. *Technical Advisory: [Rescinded] Cable Stays of Cable-Stayed Bridges*. Technical Advisory 5140.25. Washington, DC: Federal Highway Administration. https://www.fhwa.dot.gov/bridge/t514025.cfm, last accessed March 21, 2020.

16. Paredes, H., ed. 2018. *Coating Solutions for Active Corrosion Resistance*. Zwevegem, Belgium: Bekaer https://www.bekaert.com/content/dam/corporate/en/products/agriculture/fencing/pdf/Bekaert-active-corrosion-resistance%20(3).pdf, last accessed May 9, 2024.

17. ASTM. 2021. *Standard Specification for Filled Epoxy-Coated Seven-Wire Prestressing Steel Strand*. ASTM A882/A882M-20. West Conshohocken, PA: ASTM International.

18. Sumiden Wire. 2023. *Epoxy Coated and Filled Strand Questions & Answers*. https://www.sumidenwire.com/wp-content/uploads/2015/11/ECS-FAQ-2023-REV-2023-12-19.pdf, last accessed May 9, 2024.

19. ASTM. 2020. *Standard Specification for Low-Relaxation, Seven-Wire Steel, Grade 240 [1655], Stainless Steel Strand for Prestressed Concrete*. ASTM A1114/A1114M-20. West Conshohocken, PA: ASTM.

20. Lee, S-K. 2021. *Corrosivity of Water-Soluble Sulfate Ions in Simulated Grout Pore Water Solutions and Different Types of Grout Samples*. Report No. FHWA-HRT-21-052. Washington, DC: Federal Highway Administration. https://highways.dot.gov/sites/fhwa.dot.gov/files/FHWA-HRT-21-052.pdf, last accessed April 23, 2024.

Authors—This study was written by Dr. Seung-Kyoung Lee (ORCID ID 0000-0001-7367-5197).

Researchers—This study was conducted by Dr. Seung-Kyoung Lee (ORCID ID 0000-0001-7367-5197).

Distribution—This summary report is being distributed according to a standard distribution. Direct distribution is being made to the FHWA divisions and Resource Center.

Availability—This summary report may be obtained at https://highways.dot.gov/research.

Key Words—Corrosion resistant strand, flow-filled epoxy-coated strand, hot-dip galvanized strand, solid stainless steel strand.

SEPTEMBER 2024

Recommended citation: Federal Highway Administration, *Laboratory Evaluation of Five Metallic Strand Materials for Corrosion Control of Post-Tensioned Tendons: Summary of Preliminary Findings* (Washington, DC: 2024) https://doi.org/10.21949/1521601

FHWA-HRT-24-158
HRDI-30/09-24(WEB)E